CrystEngComm

Accepted Manuscript

ROYAL SOCIETY OF CHEMISTRY

www.rsc.org/crystengcomm

Faegheh Hoshyargar, Enrico Mugnaioli, Robert Branscheid, Ute Kolb, Martin Panthöfer, Wolfgang Tremel*

Structure Analysis at the Nanoscale: Closed WS_2 Nanoboxes through a Cascade of Topotactic and Epitactic Processes

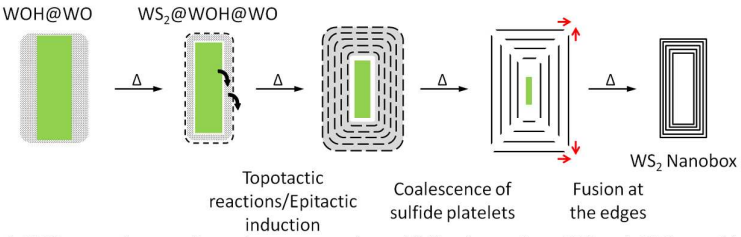

Closed WS_2 nanoboxes form by topotactic sulfidization of a WO_3 / $WO_3 \times \frac{1}{3}$ H_2O intergrowth phase. The box-like morphology can be traced back to a topotactic dehydration reaction of the precursor followed by an epitactic induction of intermediate hexagonal WO_3 which eventually serves as a template that maintains the particle box-like morphology of the resulting WS_2 nanoparticles.

Cite this: DOI: 10.1039/c0xx00000x

www.rsc.org/xxxxxx

ARTICLE TYPE

Structure Analysis at the Nanoscale: Closed WS_2 Nanoboxes through a Cascade of Topo- and Epitactic Processes

Faegheh Hoshyargar,[a] Enrico Mugnaioli,[b] Robert Branscheid,[b] Ute Kolb,[b,c] Martin Panthöfer,[a] Wolfgang Tremel[a]*

Received (in XXX, XXX) Xth XXXXXXXXX 20XX, Accepted Xth XXXXXXXXX 20XX
DOI: 10.1039/b000000x

Closed WS_2 nanoboxes form by topotactic sulfidization of a WO_3 / $WO_3 \times ⅓\ H_2O$ intergrowth precursor. Automated diffraction tomography was used to elucidate a growth mechanism of these unconventional hollow structures. By partial conversion and structural analysis of the products, each of them representing a snapshot of the reaction at a given point of time, the overall reaction could be broken down into a cascade of individual steps and each of them identified with a basic mechanism. During the initial step of the sulfidization $WO_3 \times ⅓\ H_2O$ transforms into hexagonal WO_3 whose surface allows for the epitaxial induction of WS_2. The initially formed platelets of WS_2 exhibit a preferred orientation with respect to the nanorod surface. In the final step individual layers of WS_2 coalesce to form closed shells. In essence, a cascade of several topotactic reactions leads to epitactic induction and formation of closed rectangular hollow boxes made up from hexagonal layers.

Introduction

Layered metal dichalcogenides (MQ_2, with M = Sn, Ti, Nb, Ta, Mo, W, and Q = S, Se) form a large family of materials which has been studied for several decades.[1-4] Individual monolayers of layered chalcogenides can be isolated by the "Scotch tape method" or by micromechanical cleavage.[1] The resulting two-dimensional MQ_2 sheets containing a layer of metal atoms sandwiched between two layers of chalcogen atoms are analogues of graphene[5,6] and represent the fundamental building blocks for other low-dimensional nanostructures such as inorganic fullerenes (IF) and nanotubes (NT).[7] Since their discovery by Tenne and co-workers, many routes[8-14] have been devised for the synthesis of these nested structures with various tribological,[15] mechanical,[16,17] catalytic[18] and optoelectronic[19] applications. Current technologies applying layered chalcogenides critically depend on our ability to synthesize new nanostructured materials of a controlled size and shape, and to search for new observations that could not be realized with the bulk materials. Inorganic nanotubes and inorganic fullerene-like materials do not only display new crystalline order, they also exhibit new phenomena, which cannot be engendered by their bulk analogues.

Most synthetic approaches to chalcogenide nanoparticles are based on high temperature (> 700°C) reactions of hydrogen and hydrogen sulfide or sulfur vapor with metal oxide nanoparticles or another metal precursor. In an early synthesis of NT-WS_2, short (50 nm) nanorods of $W_{20}O_{58}$ ($WO_{2.9}$) were used as starting compounds.[20] The subsequent growth and sulfidization of these nanorods at elevated temperatures (840° C) lead to the formation of WS_2 nanotubes with a length of several microns. In another two-step approach[10,20] $W_{18}O_{49}$ nanowhiskers were prepared initially by oxidation of tungsten foil, followed by reductive sulfidization to NT-WS_2. The proposed growth mechanism[7] starts from the surface of the oxide particles and proceeds inward layer by layer until the conversion to WS_2 is complete. The reaction rate is diffusion limited because of the size of the whiskers (> 50 nm). The WS_2 nanotubes obtained by sulfidizing WO_{3-x} whiskers reflect the morphology of the template, to the extent that the thickest nanotubes are highly faceted with a prismatic cross section.[21] WS_2 nanotubes decorated on their outer surfaces with IF-WS_2 nanoparticles („nanobuds") were obtained by sulfidizing W_5O_{14} ($WO_{2.8}$) nanowires.[22]

Here, we report a mechanistic study for a new type of large nested WS_2 nanoparticles that exhibit the form of rectangular hollow boxes rather than the classic spherical morphology. These cuboids possess a hollow core surrounded by walls made up of stacked layers that meet at 90° angles. This is incompatible with the hexagonal symmetry of the constituent chalcogenide layers. By taking "snap shots" of the reaction we could show the formation of these unusual WS_2 nanoboxes to proceed by topotactic sulfidization of a WO_3 / $WO_3 \times ⅓\ H_2O$ intergrowth phase at 850°C. The formation of these unconventional intermediate structures was traced step by step using X-ray powder diffraction (XRD), high-resolution transmission electron microscopy (HRTEM), nanobeam electron diffraction (NED) and automated diffraction tomography (ADT)[23-25] from the oxide precursor via the reaction intermediate to the final chalcogenide product. Its box-like morphology is shown to start with a topotactic dehydration reaction of the precursor, a $WO_3 \times ⅓\ H_2O$ [26] "crust" on WO_3 particles,[27,28] followed by epitactic induction of a hexagonal WO_3 intermediate,[29] which subsequently serves as a template for the formation of the hollow WS_2 nanoboxes of the product phase. The systematic preparation of such hollow rectangular nanostructures is a synthetic challenge. Structural defects can lead to the formation of 90° vertexes in nested fullerenes,[21,30] and rectangular tips have been observed in niobium-doped tungsten sulfide

closed-ended nanotubes[31] due to structural defects induced by the dopant or in so-called "thick" nanotubes or nanocubes.

Experimental section

Synthesis of the WO_3 nanorods. In a glovebox, 0.2 ml of tungsten (V) ethoxide ($W(OEt)_5$, ABCR, 95%) was taken into a syringe and transferred outside the box and immediately dissolved in ~ 12.5 ml of benzyl alcohol (BzOH, Sigma, 99.8%). The clear solution was transferred into a Teflon lined 50 ml stainless steel autoclave and heated at 200°C for 25 h. After this time, the autoclave was cooled back to the room temperature normally. After cooling to the room temperature, the greenish yellow precipitate was collected by centrifugation at 9000 rpm for 10 min, washed twice with ethanol and dried at 60°C.

Synthesis of the WS_2 nanoboxes. The nanorods obtained from the first step were taken in a corundum boat and kept inside a quartz tube which was flushed with Ar for 30 min prior to the heating to remove any oxygen. The corundum boat was kept at the middle of a tube furnace and heated up to 850°C at the rate of 5°C/min under constant argon flow. Just before approaching 850°C, the Ar was switched to H_2S gas with a flow rate of 40 sccm and kept at this temperature for 30 min. During the sulfidization, the H_2S flow was carefully controlled using a flowmeter. After 30 min, the furnace was cooled to ambient temperature at the rate of 5°C/min under Ar flow. The black powder obtained after cooling was collected and was used for the further characterization.

X-ray diffraction. X-ray diffraction patterns (XRD) were recorded using a Siemens D5000 diffractometer equipped with a Braun M50 position sensitive detector in transmission mode using Ge (200) monochromatized CuKα radiation. Samples were prepared between two layers of Scotch Magic Tape. Crystalline phases were identified according to the PDF–2 database using Bruker AXS EVA 10.0 software.

Transmission electron microscopy. Low resolution transmission electron microscopy was performed on a Phillips EM-420 equipped with a slow scan CCD detector (1k x 1k) and a LaB_6 electron gun operated with an acceleration voltage of 120 kV. Transmission electron microscopy (TEM) images were processed with the Gnu Image Manipulation Program GIMP Version 2.6.8 or with Image J Version 1.43u.

High resolution transmission electron microscopy (HRTEM) images, nanobeam electron diffraction (NED) patterns and energy dispersive X-ray (EDX) spectra were taken with a FEI TECNAI F30 ST electron microscope (field-emission gun, 300 kV extraction voltages) equipped with a STEM high angular annular dark field detector and an energy-dispersive X-ray (EDX) spectrometer with a Si/Li detector and an ultrathin window for elemental analysis. HRTEM and electron diffraction were recorded by a GATAN CCD camera (14-bit 794MSC, 1024 × 1024 pixels). TEM grids were prepared by dispersion of the sample in ethanol and drop casting on 300 mesh carbon coated copper grids.

Automated diffraction tomography (ADT) data acquisition was performed with the same microscope using a FISCHIONE tomography holder and the ADT acquisition module described in ref. 30-32. The ADT3D software package was used for three-dimensional diffraction volume reconstruction and visualization.

Results and discussion

Characterization of the WO_3/ $WO_3 \times ⅓ H_2O$ precursor. Tungsten oxide nanorods were prepared solvothermally by alcoholysis of $W(OEt)_5$ at 200°C for 25 h (synthetic details are given in the Supporting Information).[33] The resulting yellow-green powder was investigated by XRD, TEM and HRTEM. According to full pattern profile analysis, the XRD pattern is a superposition of the diffraction patterns of the monoclinic phase of WO_3 (approx. 55%, crystallite size 83 nm) and an orthorhombic hydrated tungsten trioxide, $WO_3 \times ⅓ H_2O$ (ca. 45%, crystallite size 72 nm) (Fig. 1a). The results of the refinement are provided in Table S1 (Supporting Information).

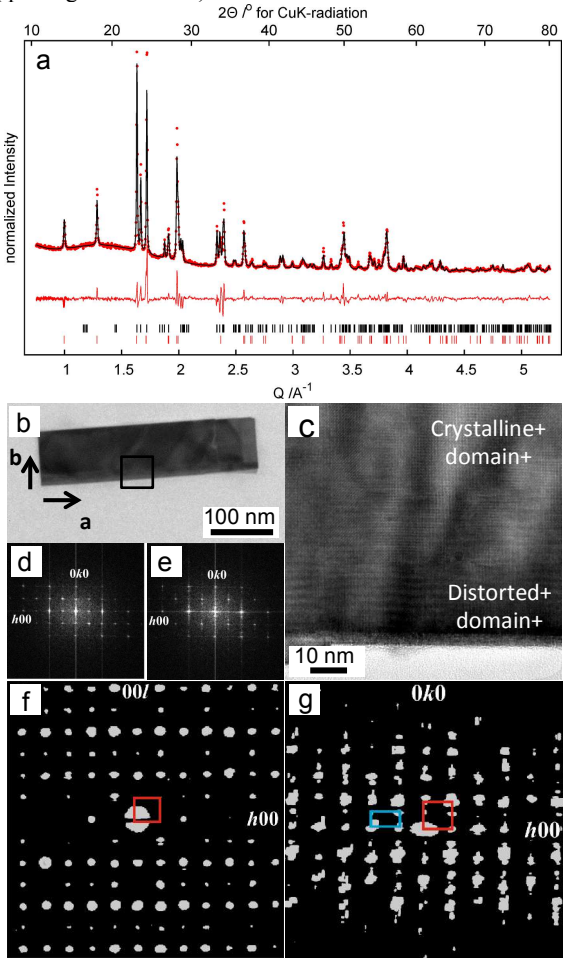

Fig. 1. WO_3 / $WO_3 \times ⅓ H_2O$ nanorod obtained from solvothermal synthesis. (a) Rietveld refinement (black line) on X-ray data (red dots) and difference (red line) for the WO_3 / $WO_3 \times ⅓ H_2O$ 2-phase model. The XRD pattern is a superposition of the diffraction patterns of the monoclinic phase of WO_3 (approx. 55%, crystallite size 83 nm, black ticks bottom trace) and an orthorhombic hydrated tungsten trioxide, $WO_3 \times ⅓ H_2O$ (approx. 45%, crystallite size 72 nm, red ticks bottom trace). (b) TEM image of a typical as-synthesized rod. (c) HRTEM of the marked area in panel b, showing a bulky crystalline domain (top) next to a more distorted domain (bottom). The distorted domain is close to the rim of the rod. (d) FFT of the ordered upper part, consistent with [001] of WO_3. (e) FFT of the rim showing diffuse scattering and reflection splitting along 0*k*0. (f) Three-dimensional ADT reconstructed diffraction volume collected on a rod and projected along b* showing how WO_3 and $WO_3 \times ⅓ H_2O$ lattices overlap in this direction. (g) Projection of the same diffraction volume along c* showing the two lattices of WO_3 (red) and $WO_3 \times ⅓ H_2O$ (blue). ADT images are realized with ADT3D software.

TEM images (Fig. 1b and Fig. S2, Supporting Information) show the typical morphology of the as-synthesized precursor. The nanorods are ca. 150 nm in width and several hundred nanometers in length, occasionally stacked and ordered along a common direction. HRTEM revealed that the inner volume of the nanorods consists of bulky crystalline domains with lattice fringes coherent with the lattice parameters of WO_3 (Fig. 1c). In contrast, regions close to the rims of the rod showed disorder features as undulated layers, faults and layer closures.

Using the ADT method we collected three-dimensional diffraction data from single nanorods, in order to achieve a deeper structural understanding of these nanocomposites. ADT reconstructed diffraction volumes (Fig. 1f, g) revealed that a typical rod consists in fact of two different intergrown lattices, corresponding to the crystal structures of WO_3 (space group $P2_1/n$, a=7.297Å, b=7.539Å, c=7.688Å, β=90.91°)[28] and $WO_3 \times \frac{1}{3} H_2O$ (space group $Fmm2$, a=7.359Å, b=12.513Å, c=7.704Å).[26] The two lattices have related cell vectors with approximately the same orientation and can be distinguished only by the different length of **b***. The main growth direction of the rods is always [100].

This result is supported by the analysis of the fast Fourier transforms (FFT) of HRTEM images collected along [001] (Fig. 1d-e). The FFT's from areas with enhanced disorder show a progressive weakening of reflections ($0kl$) with $k+l$ = 2N+1 (consistent with the F-centred Bravais lattice of $WO_3 \times \frac{1}{3} H_2O$) and diffuse scattering appears along **b***, i.e orthogonal to the main growth direction. The disordered areas correspond therefore to the hydrated areas ($WO_3 \times \frac{1}{3} H_2O$) and are always localized closer to the rim of the nanorod.

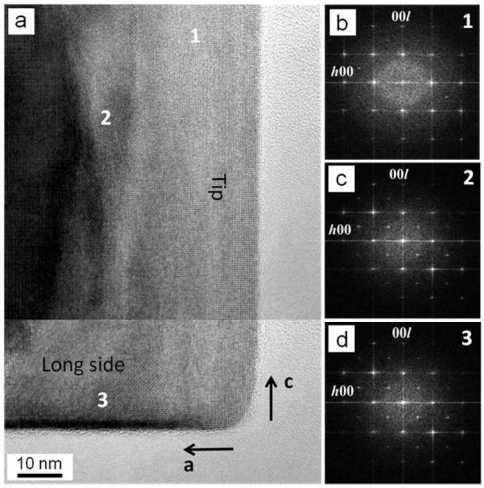

Fig. 2. HRTEM image and FFTs of a nanorod oriented along [010], FFTs from the areas (b) area 1 – (100) facet, (c) area 2 – inner part, (d) area 3 – (001) facet.

Fig. 2a shows a second rod, oriented along [010]. In the center, where WO_3 is exclusively present, the extinction rule for ($h0l$) is $h+l$ = 2N, consistent with space group $P2_1/n$ (Fig. 2c). The same feature was observed close to the 001 facet, which apparently is not affected by the hydration (Fig. 2d). In contrast, close to the 100 facet the extinction rule for ($h0l$) is h,l = 2N, consistent with space group $Fmm2$, i.e. $WO_3 \times \frac{1}{3} H_2O$ (Fig. 2b). This means that the transformation from WO_3 to $WO_3 \times \frac{1}{3} H_2O$ is structurally controlled and proceeds faster through the 100 and 010 facets and slower on the 001 facets. This can be explained considering WO_3 as a layered structure with oxygen bridges stacked along [001], water intercalates rapidly into the layers, replacing some oxygen atoms and expanding the b axis. In comparison, the hydration orthogonal to the layer proceeds slowly.

Characterization of the WS_2 nanoboxes. Previously, we had elaborated the complete oxide to sulfide conversion method to synthesize very long (several hundred μm) WS_2 nanotubes by sulfidization of WO_3 nanorods.[27] Here, in the presence of the WO_3 / $WO_3 \times \frac{1}{3} H_2O$ intergrowth phases, the sulfidization with H_2S leads to a full conversion of the oxide precursor into hollow WS_2 nanoboxes. In contrast, the sulfidization of pure WO_3 nanorods yields exclusively WS_2 nanotubes.[27] As shown in Fig. 3a, the X-ray powder diffraction pattern obtained after sulfidization matches with that of a mixture of the 2H-WS_2 and the 3R-WS_2 phases. The details concerning the refinement are provided in Table S2 (Supporting Information). A slight lattice expansion of 0.3% and 1.7% along the [001] stacking direction was observed for 3R-WS_2 and 2H-WS_2, respectively.

The sulfidization of the tungsten oxide nanorods resulted in the formation of nanoboxes with approximately the same dimensions as for the oxide precursor. Two nanoboxes are displayed in Fig. 3b-c. The WS_2 nanoboxes are remarkable because (i) their apexes systematically form 90° angles as shown in Fig. 3d, but also because (ii) they are significantly larger than closed-tipped nanotubes. An EDX analysis confirmed the presence of W and S. The inner portion of the nanoboxes delivered a weaker signal, which indicated an empty or less dense core (Fig. 3e). Additionally, a weak oxygen signal was detectable from the inner part.

NED patterns showed the external walls of the nanoboxes to contain only layered WS_2 with typical interlayer distances of 0.63 nm. 3D diffraction information was obtained by ADT from an area with an atypically thick wall. These data showed that the so-synthesized WS_2 crystallize in a hexagonal lattice (Fig. 3f-g). Despite a strong diffuse scattering along **c***, the main periodicity revealed that 3R-WS_2 is the predominant polytype.[32]

In contrast, the inner part of the boxes produced a ring-like diffraction pattern that could be indexed with $hk0$ reflections of WS_2 (Fig. 3h). Upon tilting the sample the circular rings changed to ellipses (Fig. 3i). Therefore top and bottom "deck" of the boxes contain layers of WS_2 stacked with a diffuse turbostratic disorder, i.e. all layers are stacked along [001] with random **a** and **b** orientations. The internal volume of the box did not yield diffraction intensities; we can therefore assume that it is empty or amorphous. The weak oxygen EDX signal indicated the presence of minor oxide contaminations inside the nanoboxes.

In order to understand the formation mechanism of the WS_2 nanoboxes, we reduced the duration of the sulfidization; the intermediate products were collected after 10 and 20 min. HRTEM studies of the intermediates revealed that the faces of the boxes were present but contained fewer layers and were not continuous along the perimeter of the boxes (Fig. 4a). NED and EDX were comparable with those of the final product. No diffraction spots from phases other than WS_2 were detected. EDX spectra showed the presence of O, S and W; the W and S signals increased in correspondence of well-developed chalcogenide layers (Fig. 4b). Complete nanoboxes have formed after 30 min. Prolonged sulfidization did not change the morphology or phase purity of the nanoboxes.

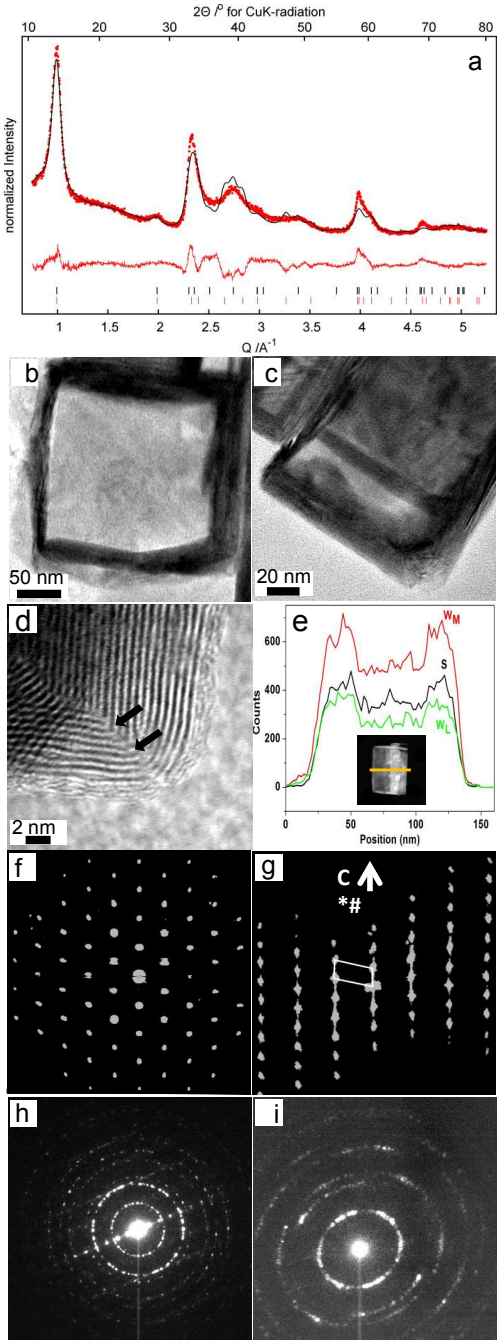

Fig. 3. (a) Rietveld refinement (black line) on X-ray data (red dots) and difference (red line) for the product obtained after sulfidization of the oxide nanorods (black). The XRD pattern is a superposition of the diffraction patterns of 2H-WS_2 (approx. 41%, crystallite size 10 nm, black ticks bottom trace) and 3R-WS_2 (approx. 59%, crystallite size 10 nm, red ticks bottom trace). (b,c) TEM images of typical nanoboxes; (d) HRTEM showing the right angle at the edge of a box; (e) EDX profile across the box shown in the STEM image in the inset; (f) three-dimensional ADT reconstructed diffraction volume collected on a wall and projected along c*; (g) the same diffraction volume showing the diffuse scattering along c* and the rhombohedral arrangement of the prominent reflections. (h) NED from a box collected at 0° tilt. The rings correspond to the *hk0* reflection of WS_2 and originate from the bottom of the box, while the line of reflections originates from a wall, corresponding to an interlayer distance of 0.63 nm (typical for WS_2 layers). (i) NED from the internal volume of a box after a tilt of 20°, where the diffraction rings corresponding to the *hk0* reflections turn into ellipses due to the oblique cut.

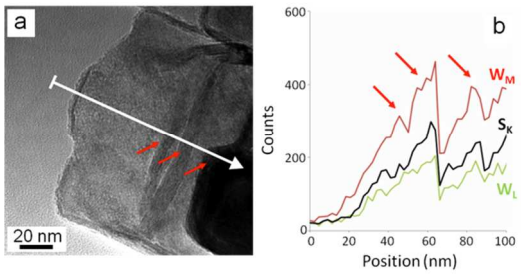

Fig. 4. Reaction intermediate of the sulfidization process. (a) HRTEM image showing a thin WS_2 layer forming around a box. The arrow indicates the trace of the EDX profile shown in panel b. (b) EDX profile showing the increasing of the S and W signal intensities in correspondence of well-developed chalcogenide layers (marked by small red arrows).

Growth mechanism. The proposed growth scenario is illustrated in Fig. 5. Sulfidization of monoclinic WO_3 leads to the formation of WS_2 without crystallographic relation between the oxide precursor and the WS_2 product. This is observed frequently in octahedral,[25,34] and onion type fullerenes.[7,8] The intermediate step involves a "weathering" of the monoclinic WO_3 surface in a topotactic reaction to $WO_3 \times \frac{1}{3} H_2O$. The subsequent topotactic dehydration of $WO_3 \times \frac{1}{3} H_2O$ to hexagonal WO_3[35] leads to the formation of nanorods whose surface allows for the epitaxial induction of WS_2. Initially formed platelets of WS_2 exhibit a preferred orientation with respect to the nanorod surface; yet they do not wrap the nanorods completely which allows for an ongoing conversion of the high density WO_3 cores (0.075 atoms/Å^3) into WS_2 (density 0.055 atoms/Å^3). However, the formation of $WO_3 \times \frac{1}{3} H_2O$ and, hence, the subsequent epitaxial induction is faster on 100 and 010 facets and slower on 001 facets of the precursor. The former lead to the formation of well-developed chalcogenide walls on the four box sides, while the latter, corresponding to box floor and roof, give origin to thinner chalcogenide layers affected by rotational disorder. After full conversion, the individual WS_2 platelets coalesce to closed shells in order to reduce the overall number of dangling bonds. At the tips of the former WO_3 rods this leads to the formation of 90° kinks (arrows in Fig. 3d) which finally leads to the formation of hollow rectangular WS_2 boxes.

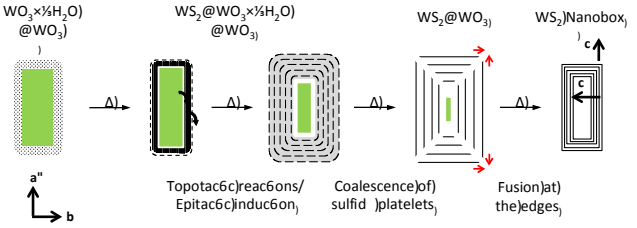

Fig. 5. Proposed formation mechanism of the WS_2 nanoboxes.

Conclusions

Layered metal chalcogenide nanoparticles have great potential in tribological, mechanical or catalytic applications. Solid state reactions leading to metal chalcogenide nanoparticles may be very complex and proceed via a series of steps, although the basic mechanism comprising the overall reaction may appear quite

simple. This was demonstrated here through the formation of hollow rectangular WS_2 nanoboxes with an unusual morphology. By partial conversion and structural analysis of the products, each of them representing a snapshot of the reaction at a given point of time, the overall reaction could be broken down into a cascade of several individual steps and each of them identified with a basic mechanism: (i) During the initial steps of the sulfidization, $WO_3 \times ⅓\ H_2O$ transforms into h-WO_3 whose surface allows (ii) for the epitaxial induction of WS_2. (iii) Initially formed platelets of WS_2 exhibit a preferred orientation with respect to the nanorod surface. (iv) Finally, the individual layers of WS_2 coalesce to form closed shells. In essence, a cascade of several topotactic reactions leads to epitactic induction and formation of closed rectangular hollow boxes made up from hexagonal layers.

The present study on the formation of hollow rectangular WS_2 nanoboxes shows that solid state reactions may be mechanistically very complex. The combination of X-ray diffractometry and automated diffraction tomography (ADT) allowed a deeper structural understanding of the role of a hydrated tungsten oxide $WO_3 \times ⅓\ H_2O$ during the formation of hollow WS_2 nanoparticles. In previous work[35] the participation of a hydrated oxide phase in the sulfidization process was postulated, but could neither be identified nor structurally be characterized. This study allows for the first time a detailed mechanistic understanding of a multistep solid state transformation in a polycrystalline nanocomposite and of an unexpected complex growth mechanism at the nanoscale.

Acknowledgements

This research was partially supported by the Deutsche Forschungsgemeinschaft (DFG) within the priority programs 1415 "Kristalline Nichtgleichgewichtsphasen". The facilities of the Electron Microscopy Center in Mainz (EZMZ) were supported by the State Excellence Cluster COMATT, the SFB 625 and the Stiftung Rheinland Pfalz für Innovation.

Notes

[a]*Institut für Anorganische Chemie und Analytische Chemie, Johannes Gutenberg-Universität, Duesbergweg 10-14, D-55099 Mainz, Germany. Fax: +49-6131-39-25605; Phone: +49-6131-39-25135; E-mail: tremel@uni-mainz.de*

[b]*Institut für Physikalische Chemie, Johannes Gutenberg-Universität, Duesbergweg 10-14, D-55099 Mainz, Germany.*

[c]*Institut für Angewandte Geowissenschaften, Technische Universität Darmstadt, Schnittspahnstrasse 9, 64287 Darmstadt, Germany*

† Electronic Supplementary Information (ESI) available: (1) Table S1: Measurement and refinement parameters of the x-ray diffraction pattern of the WO_3 / $WO_3 \times ⅓\ H_2O$ precursor. (2) Measurement and refinement parameters of the x-ray diffraction pattern of the product after sulfidization. (3) TEM and HRTEM overview images of two rods of the WO_3 / $WO_3 \times ⅓\ H_2O$ precursor (4) TEM overview image of the sulfidized WS_2 product. See DOI: 10.1039/b000000x/

References

1. J. A. Wilson and A. D. Yoffe, *Adv. Phys*. 1969, **18**, 193-335.
2. J. A. Wilson, F. J. Di Salvo and S. Mahajan, *Adv. Phys.* 1975, **24**, 117-201.
3. K. Rossnagel, *J. Phys.: Condens. Matter* 2011, **23**, 213001.
4. R. Tenne and M. Redlich, *Chem. Soc. Rev*. 2010, **39**, 1423-1434.
5. B. Radisavljevic, A. Radenovic, J. Brivio, V. Giacometti and A. Kis, *Nature Nanotechnol*. 2011, **6**, 147-150.
6. C. N. R. Rao and A. Nag, *Eur. J. Inorg. Chem.* 2010, 4244-4250.
7. R. Tenne, L. Margulis, M. Genut and G. Hodes, *Nature* 1992, **360**, 444-446.
8. Y. Feldman, E. Wasserman, D. J. Srolovitz and R. Tenne, *Science* 1995, **267**, 222-225.
9. M. Remskar, Z. Skraba, M. Regula, C. Ballif, R. Sanjines and F. Levy, *Adv. Mater.* 1998, **10**, 246-249.
10. Y. Q. Zhu, W. K. Hsu, N. Grobert, B. H. Chang, M. Terrones, H. Terrones, H. W. Kroto, D. R. M. Walton and B. Q. Wei, *Chem. Mater.* 2000, **12**, 1190-1194.
11. R. Sen, A. Govindaraj, K. Suenaga, S. Suzuki, H. Kataura, S. Iijima and Y. Achiba, *Chem. Phys. Lett*. 2001, **340**, 242-248.
12. J. Etzkorn, H. A. Therese, F. Rocker, N. Berntsen, U. Kolb and W. Tremel, *Adv. Mater*. 2005, **17**, 2372-2375.
13. A. Margolin, F. L. Deepak, R. Popovitz-Biro, M. Bar-Sadan, Y. Feldman and R Tenne, *Nanotechnology* 2008, **19**, 095601.
14. A. Yella, E. Mugnaioli, M. Panthöfer, H. A. Therese, U. Kolb and W. Tremel. *Angew. Chem.* 2009, **121**, 6546-6551; *Angew. Chem. Int. Ed.* 2009, **48**, 6426-6430.
15. M. Redlich, A. Gorodnev, Y. Feldmean, I. Kaplan-Ashiri**,** R. Tenne, N. Fleischer, M. Genut and N. Feuerstein, *J. Mater. Res.* 2008*,* **23**, 2909-2915.
16. M. Naffakh, M. Remskar, C. Marco, M. A. Gomez-Fatou and I. Jimenez, *J. Mater. Chem*. 2011, **21**, 3574-3578.
17. I. Kaplan-Ashiri, S. R. Cohen, K. Gartsman, V. Ivanovskaya, T. Heine, G. Seifert, I. Wiesel, H. D. Wagner and R. Tenne. *Proc. Natl. Acad. Sci*. 2006, **103**, 523-528.
18. Y. Tsverin, R. Popovitz-Biro, Y. Feldman, R. Tenne, M. Komarneni, Z. Yu, A. Chakradhar, A. Sand and U. Burghaus, *Mater. Res. Bull.* 2012, **47**, 1653–1660.
19. R. Kreizman, O. Schwartz, Z. Deutsch, S. Itzhakov, A. Zak, S. R. Cohen, R. Tenne and D. Oron, *Phys. Chem. Chem. Phys*. 2012, **14**, 4271-4275.
20. A. Rothschild, J. Sloan and R. Tenne, *J. Am. Chem. Soc*. 2000, **122**, 5169-5179.
21. A. Rothschild, R. Popovitz-Biro, O. Lourie and R. Tenne, *J. Phys. Chem. B*, 2000, **104**, 8976-8981.
22. M. Remskar, M. Virsek and A. Jesih, *Nano Lett*. 2008, **8**, 76-80.
23. U. Kolb, T. Gorelik, C. Kubel, M. T. Otten, D. Hubert, *Ultramicroscopy* 2007, **107**, 507-513.
24. U. Kolb, T. Gorelik and M. T. Otten, *Ultramicroscopy* 2008, **108**, 763-772.
25. E. Mugnaioli, T. Gorelik and U. Kolb, *Ultramicroscopy* 2009, **109,** 758-765.
26. B. Gerand, G. Nowogrocki, and M. Figlarz, *J. Solid State Chem.* 1981, **38**, 312-320.
27. H. A. Therese, J. Li, U. Kolb and W. Tremel, *Solid State Sci.* 2005, **7**, 67-72.
28. B. Loopstra and P. Boldrini, *Acta Crystallogr.* 1966, **21,** 158-162.
29. A. Yella, E. Mugnaioli, M. Panthöfer, U. Kolb and W. Tremel, *Angew. Chem.* 2010, **122**, 3373-3377; *Angew. Chem. Int. Ed.* 2010, **49**, 3301-3305.
30. S. Bastide, D. Duphil, J.-P. Borra and C. Levy-Clement. *Adv. Mater.* 2006, **18**, 106-109.
31. Y. Q. Zhu, W. K. Hsu, H. Terrones, N. Grobert, B. H. Chang, M. Terrones, B. Q. Wei, H. W. Kroto, D. R. M. Walton, C. B. Bothroyd, I. Kinloch, G. Z. Chen, A. H. Windle and D. J. Fray, *J. Mater. Chem.* 2000, **10**, 2570-2577.
32. W. J. Schutte, J. L. De Boer and F. Jellinek, *J. Solid State Chem.* 1987, **70**, 207-209.
33. J. Polleux, A. Gurlo, N. Barsan, U. Weimar, M. Antonietti, M. Niederberger, Angew. Chem. 2005, **118**, 267-271; *Angew, Chem. Int. Ed*. 2005, **45**, 261-265.
34. A. Albu-Yaron, M. Levy, R. Tenne, R. Popovitz-Biro, M. Weidenbach, M. Bar-Sadan, L. Houben, A. N. Enyashin, G. Seifert, D. Feuermann, E. A. Katz and J. M. Gordon, *Angew. Chem*. 2011, **123**, 1850-1854; *Angew. Chem. Int. Ed.* 2011, **50**, 1810-1814.
35. B. Gerand, G. Nowogrocki, J. Guenot and M. Figlarz, *J. Solid State Chem.* 1979, **29**, 429-434.
36. A. Zak, L. Sallacan-Ecker, A. Margolin, M. Genut and R. Tenne, *Nano* 2009, **4**, 91–98.